1991 SCA Conference Paper Number 9113

FLUID VELOCITIES IN OIL CORES DURING WATER INJECTION

M. A. Robinson (1), W. A. Edelstein (2)

(1) Chemical Engineering Department, University of Houston, Houston, Texas 77004 and University of Wyoming, Laramie, Wyoming 82071.
(2) General Electric Corporate Research & Development, Schenectady, New York 12301.

INTRODUCTION

In most coreflood experiments, a fluid is injected in one end of the core and produced and measured at the other end. Such an experiment gives little information about the nature of the pore structure. Instead, it can only yield averaged properties for the entire core.

With the advent of non-invasive imaging techniques (X-ray CT Scanning and Magnetic Resonance Imaging), it has become possible to observe the 3-dimensional structure of the core during corefloods (see Majors, *et al*, for example). Properties such as local porosities, saturations, and velocities can be determined inside the core, potentially yielding much useful information on the nature of the fluid displacement.

In the past, X-ray CT Scanners have been used in flow imaging experiments on oil cores. However, such experiments required displacement of the resident fluid with a fluid of different X-ray absorptivity, and local velocity could only be calculated indirectly at the front. With MRI it is possible to measure fluid velocities at any point within the core with only a single flowing phase: no displacement front is required. The measurements are done in the steady-state mode, so no local pressure and saturation transients are produced.

Using MRI to measure fluid velocities inside oil cores is extremely difficult. Because of high mineral content and high surface-to-volume ratios inside oil cores, the T_2 relaxation constant is quite short. In order to measure velocities accurately, pulse sequences with very short spin-echo times are required. In addition, the signal-to-noise ratio for core imaging experiments is only on the order of 10:1. Unless the flow rate is quite high inside the core, the effect of low signal-to-noise ratio on the velocity measurement can be catastrophic. Because of these conditions, long experiments are required in order to get adequate signal-to-noise. A modified 3DFT pulse sequence is used in order to obtain the shortest echo times possible, and yet have a sufficiently long flow encode time in order to measure the slow velocities observed in core flood experiments.

The use of a 3DFT pulse sequence yields a complete dataset for the core, so that the velocity images can be viewed in all three coordinate directions at various positions within the core.

EXPERIMENTAL

The three-dimensional Fourier Transform (3DFT) flow pulse sequence shown in Figure 1 has two directions of phase encoding. The phase encoding in the GS-direction has 16 steps and defines 16 slices that can be viewed following reconstruction. The advantage of the 3DFT sequence is that a short rectangular 90 degree radiofrequency (RF) pulse can be used, which saves time compared to a slice-selective sin(x)/x pulse in a 2DFT sequence. For example, our 90 degree RF pulse is only 47 μsec long, whereas the typical 90 degree selective RF pulse lasts a millisecond or longer. 3DFT takes longer than 2DFT - a 16-slice 3DFT takes 16 times as long as a single-slice 2DFT sequence - but the additional time improves our signal-to-noise ratio, which is particularly important in the present case.

Flow encoding gradient lobes are positioned on each side of the 180° pulse, in order to maximize the flow encode time while minimizing the echo time. Such a configuration requires a very accurate 180° pulse, so that the NMR effect of the flow encode gradients is zero for non-moving spins. The parameters for the pulse sequence are shown in Table 1 for the two cores which were studied.

The experiments were conducted using a General Electric CSI *Omega* 2-tesla imager with a 31 cm magnet bore. The system is equipped with *Acustar* shielded gradient coils with strengths of up to 20 G/cm. The use of shielded gradients is recommended, because they elicit smaller eddy currents, thus improving the accuracy of the flow measurements. A 10.8 cm bird-cage RF coil tuned to protons (85 MHz) was used. Bird-cage coils are preferable, because they yield images with less intensity artifacts due to RF inhomogeneity than the more commonly used saddle coil (see Hayes, *et al*).

Two oil cores were studied during water injection: Casper sandstone and San Andres dolomite. The Casper sandstone is very layered and contains high amounts of iron, causing a small T_2 value of 5.365 ms. It has a permeability in the range of 77-88 md, and a porosity of 16.1%. The porosity distribution for the core, determined using MRI, is shown in Figure 2.

The San Andres dolomite is very heterogeneous, containing tight regions with almost no permeability, as well as vuggy regions of very high permeability. The T_2 is 35.0 ms, considerably longer than that of the Casper sandstone. It has a permeability of 10-60 md, and an average porosity of approximately 16%. The porosity distribution for this core is shown in Figure 3. The broad, skewed distribution is indicative of the heterogeneity of this core.

In lieu of core holders, end caps were placed on the cores, and the cores were wrapped in fiberglass and epoxy in order to allow injection of water at relatively high flow rates. It is estimated that such a configuration can withstand pressures up to 150 psi.

THEORY

The velocity of the flow is measured in terms of the phase of the transverse spin magnetization. The phase shift in a voxel due to fluid moving with a constant velocity component V_i in the *i* coordinate direction is given by the equation

$$\varphi = \gamma m_1 V_i \tag{1}$$

where m_1 is the first moment of the gradient:

$$m_1 = \int t\, G_i(t)\, dt \qquad (2)$$

For the bipolar, trapezoidal gradients used in these experiments, Equation 1 simplifies to

$$\varphi = \gamma\, G_i\, \Delta\, (\text{flowt} + \text{rt})\, V_i \qquad (3)$$

where Δ is the time separation between the gradient pulses, rt is the ramp time of the pulse, flowt is the duration of the pulse, and G_i is the magnitude of the pulse (see Figure 1). From Equation 3, it is seen that the phase shift in each voxel is directly proportional to the velocity of the fluid in that voxel. In order to measure slow flow, G_i must be quite large. However, if the flow is too fast, the phase shift will be greater than π and wrap around to $-\pi$, causing high positive flow to appear as negative in the phase image.

Unfortunately, one can not simply image the flow and obtain the velocity directly using Equation 3. Because of eddy currents and other effects, it is helpful to have data to reference with the given phase. For that reason, two datasets are obtained: one with no flow going through the core, and the second with the flow turned on. The phase difference between the two images is used as φ in Equation 3.

Because a 3DFT pulse sequence is used, a third Fourier transform is performed. In order to measure accurate values for the phase, a sufficient number of points must be obtained in all three dimensions. Thus, a minimum of sixteen phase encode steps must be used.

It is possible to obtain all three components of the velocity vector by performing three experiments, using the three orthogonal gradients to flow encode the x-, y-, and z-directional flow. For this work, only the flow in the z-direction (axial flow) is discussed.

RESULTS

Casper Sandstone

Figures 4-18 show various images of Casper sandstone. Figure 4 shows a transverse (x,y) slice near the inlet to the core. The proton signal is proportional to porosity. The layers in Casper sandstone are clearly visible as areas of varying signal intensity.

Figure 5 shows an image of the positive flow through this slice. The gray scale in the image ranges from black for no positive flow, to white for velocities of 0.038 cm/sec or greater. The velocity appears uniform across most of the slice (the layers do not appear in the flow image except in the upper right), indicating piston-like displacement. This image suggests that the flow is not fully developed at this point in the core (see below).

Figure 6 shows an image of the negative flow in this slice. There are several regions where the flow appears to be negative, including a long layer in the lower left of the core. In theory, the bulk of the flow should be positive, because of the application of a pressure gradient in the +z direction. Thus, the results shown here are counter-intuitive. Subsequent one-dimensional experiments seem to support the notion that backflow is occurring, and we hope to perform future 3DFT experiments to confirm this.

Figure 7 shows the magnitude image for a second transverse slice, located 27 mm from the slice shown in Figure 4. The high porosity region in the lower left hand corner remains. Figure 8 shows the positive flow image, and Figure 9 shows the negative flow. In this case, the layers are becoming more apparent in the flow image, and the flow appears to mirror the magnitude (porosity) image, showing that once the flow has developed, it preferentially channels into the high porosity regions (regions of high porosity elicit higher flow rates). The backflow region is still apparent in this slice (Figure 9).

Figures 10-12 show the magnitude and velocity images for a third slice, 27 mm further from the inlet. The velocity image again appears to mirror the porosity image, and the backflow region persists.

Figures 13-15 show a sagittal (y, z) slice and Figures 16-18 show a coronal (x, z) slice near the center of the core. There appears to be very little negative flow, and the displacement appears piston-like.

San Andres Dolomite

Figures 19-30 show various images of San Andres dolomite. Figure 19 shows a transverse slice taken near the inlet to the core. The heterogeneity of the core is visible as areas of varying signal intensity. The white regions correspond to high porosity, vuggy regions, while the grayer areas are regions of very low porosity.

Figure 20 shows an image of the positive flow through this slice. There is no negative flow, as indicated in Figure 21. The velocity in this slice is fairly uniform, indicating piston-like displacement near the entrance to the core. However, the top of the core shows a slightly enhanced flow rate.

Figure 22 shows the magnitude image for a second transverse slice, located 21 mm from the slice shown in Figure 19, near the center of the core. It is more heterogeneous than the slice shown in Figure 19. Figure 23 shows the positive flow through this slice, while Figure 24 shows the negative flow. In this case, the flow appears to be channeling into a few high porosity regions, leaving some regions of the cross-section unswept. The region of higher flow at the top of the core persists, suggesting a channel where the epoxy broke away from the core.

Figure 25 shows the magnitude image for a sagittal slice near the center of the core. The intensity of the image fades near the ends, due to the length of the core, which takes it outside the homogeneous region of the RF field.

Figure 26 shows the positive flow image for this slice, and Figure 27 shows the negative flow. The effects of the low signal-to-noise ratio are apparent at the ends of the core, especially in the negative flow image, which appears to be dominated by noise. The positive flow image shows that the flow in this slice is high near the inlet to the core (bottom of image), but fades away near the center. The second half of the core is not swept by the flow, except for some possible backflow. This is because of a channel at the right-hand edge of the core, which appears as a bright white line. This is the same channel that was apparent at the top in Figures 20 and 23.

Figures 28-30 show a coronal slice taken near the center of the core. Again, low signal-to-noise ratio is a problem, especially near the exit from the core. The positive flow image indicates that the second half of the core was not swept beyond the region where the channel occurred.

CONCLUSIONS

A method has been presented for the measurement of flow velocities during water injection into porous rocks. Although it has only been applied to measure axial flow through the cores, the same pulse sequence can be utilized to measure transverse flow, yielding a complete picture of the displacement process.

The use of a 3DFT flow pulse sequence yields a complete dataset for the core. With the proper software, a 3-dimensional map of the flow velocities can be constructed. In addition, it should be possible to correlate the porosities and velocities at any point within the core. Preliminary results show that flow through a porous rock is highest in regions of high porosity. The images show that when the flow has had time to develop, the high velocity regions correspond to regions of high porosity in the core.

The experimental results demonstrate the ability of MRI to detect flow anomalies such as channels, and thus, MRI could be of great use in the interpretation of coreflood experiments.

ACKNOWLEDGEMENT

This material is based upon work supported under a National Science Foundation Graduate Fellowship.

REFERENCES

Hayes, C. E., *et al*, *J. Magn. Reson.* **63**, 622 (1985).
Majors, P. D., *et al*, *J. Magn. Reson.* **89**, 470 (1990).

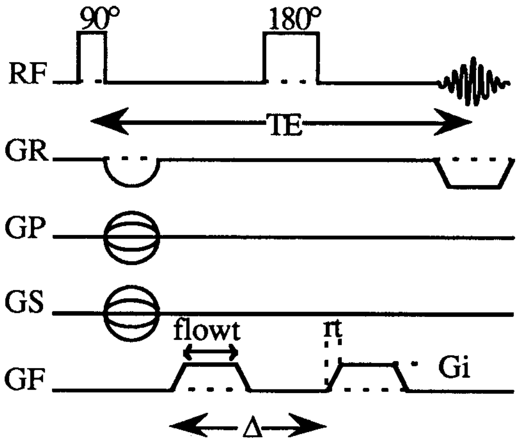

Figure 1 - 3DFT Flow Pulse Sequence

Table 1 - Flow Imaging Parameters

Type of Oil Core	Casper	San Andres
Number of averages	32	32
Recycle time (sec)	0.45	0.45
Number of slices	16	16
Axial field of view (mm)	144	112
Image field of view (mm)	80	80
Image resolution	64	64
Echo time (msec)	15	15
Flow gradient (G/cm)	14.6	14.6
flowt (msec)	6.477	6.477
rt (msec)	0.175	0.175
Δ (msec)	7.025	7.025

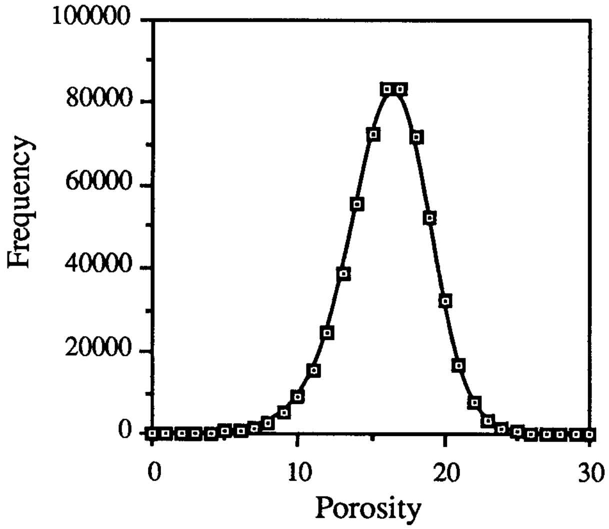

Figure 2 - Casper Sandstone
Porosity Distribution

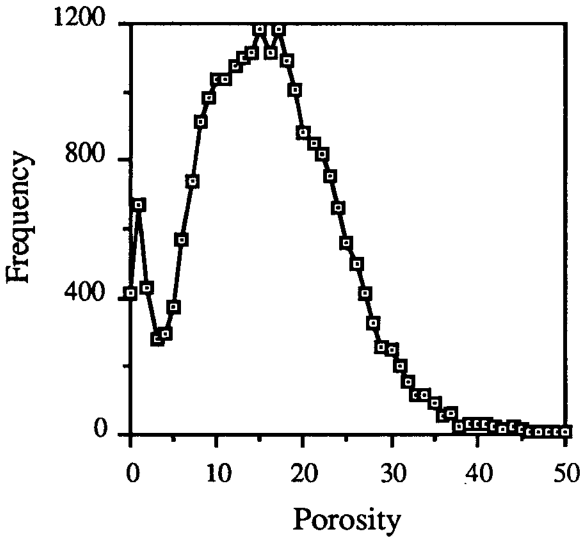

Figure 3 - San Andres Dolomite
Porosity Distribution

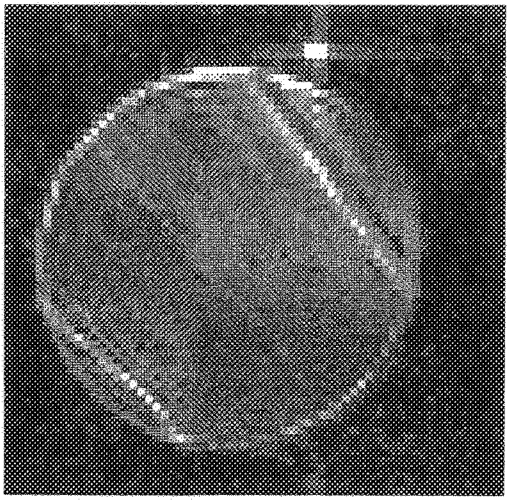

Figure 4 - Casper Sandstone Slice 4
Magnitude Image

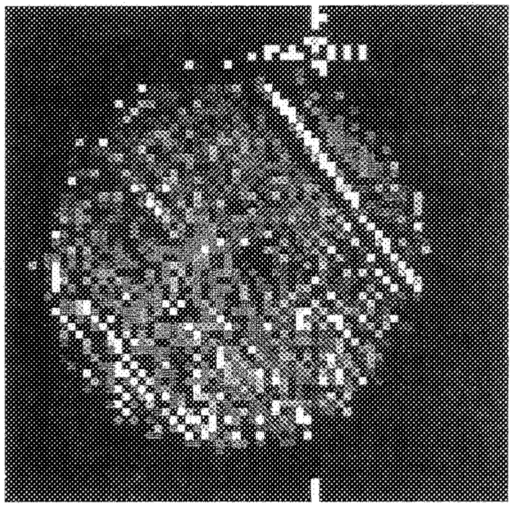

Figure 5 - Casper Sandstone Slice 4
Positive Flow Image

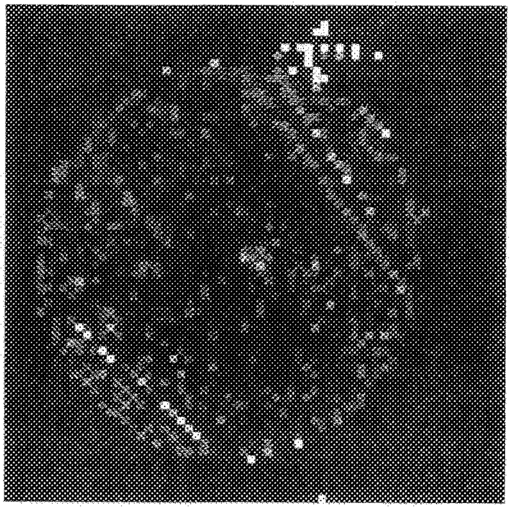

Figure 6 - Casper Sandstone Slice 4
Negative Flow Image

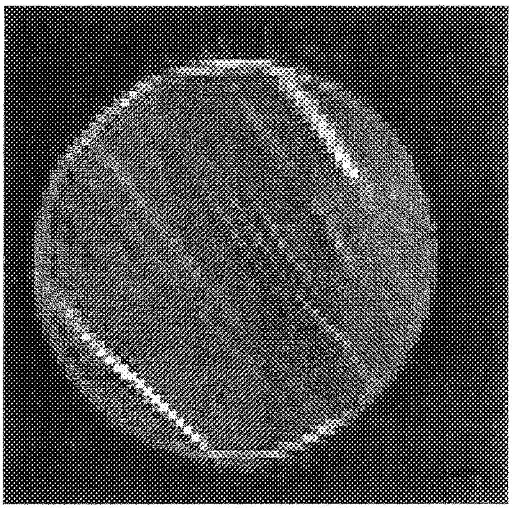

Figure 7 - Casper Sandstone Slice 7
Magnitude Image

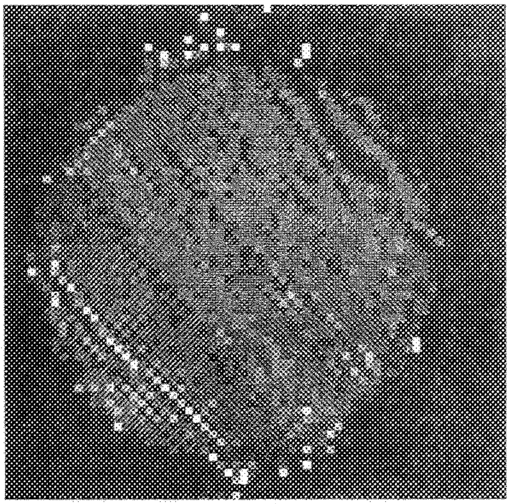

Figure 8 - Casper Sandstone Slice 7
Positive Flow Image

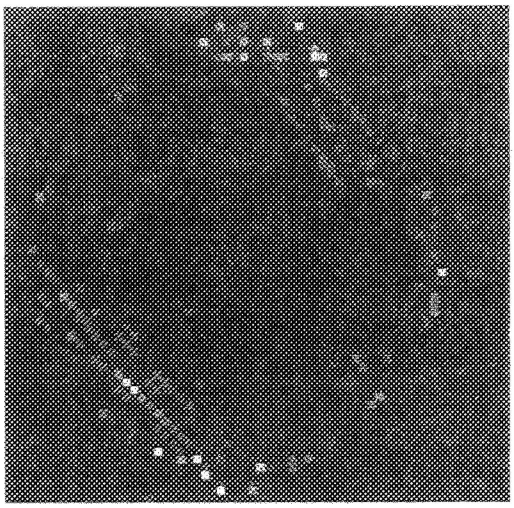

Figure 9 - Casper Sandstone Slice 7
Negative Flow Image

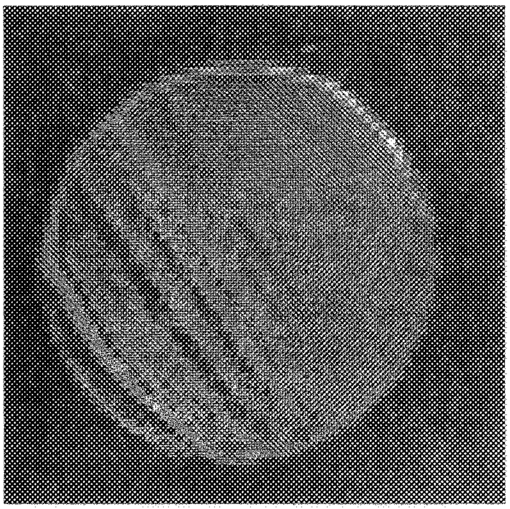

Figure 10 - Casper Sandstone Slice 10
Magnitude Image

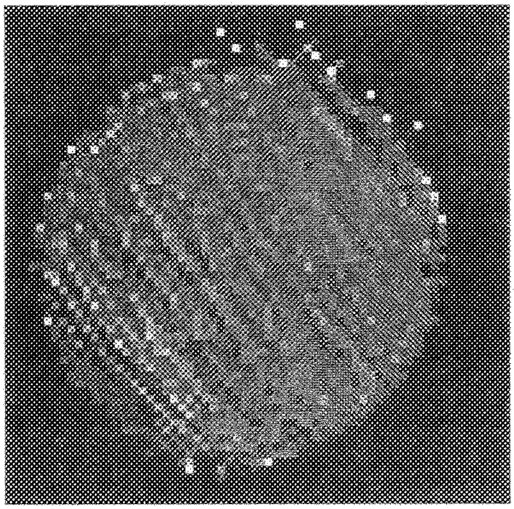

Figure 11 - Casper Sandstone Slice 10
Positive Flow Image

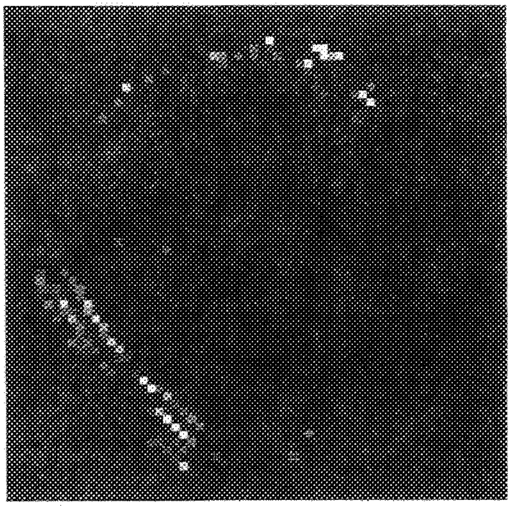

Figure 12 - Casper Sandstone Slice 10
Negative Flow Image

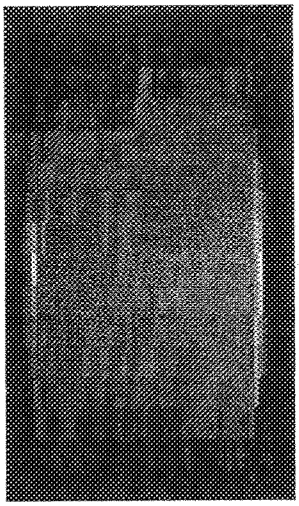

Figure 13 - Casper Sandstone Sagittal Slice
Magnitude Image

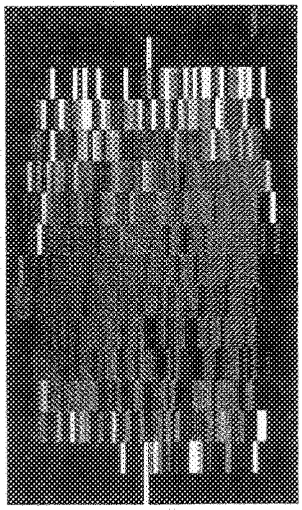

Figure 14 - Casper Sandstone Sagittal Slice
Positive Flow Image

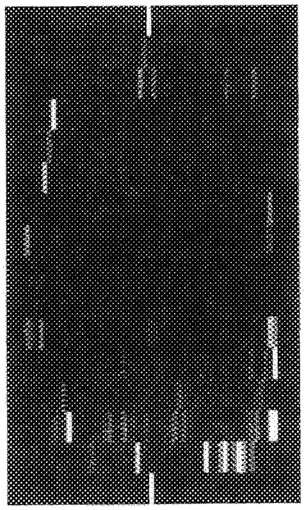

Figure 15 - Casper Sandstone Sagittal Slice
Negative Flow Image

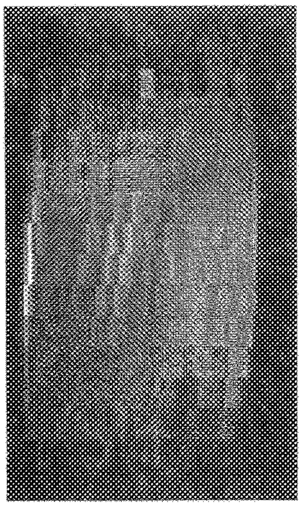

Figure 16 - Casper Sandstone Coronal Slice
Magnitude Image

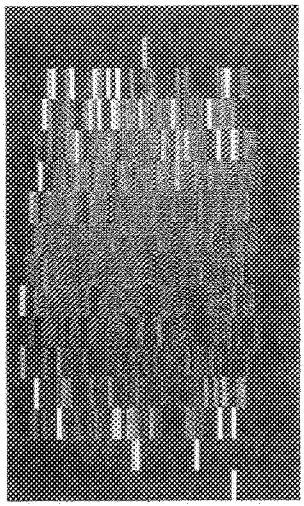

Figure 17 - Casper Sandstone Coronal Slice
Positive Flow Image

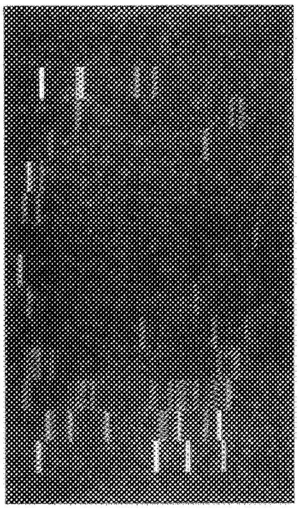

Figure 18 - Casper Sandstone Coronal Slice
Negative Flow Image

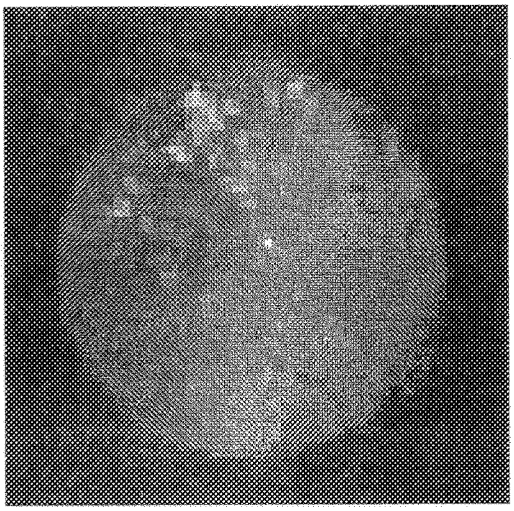

Figure 19 - San Andres Dolomite Slice 4
Magnitude Image

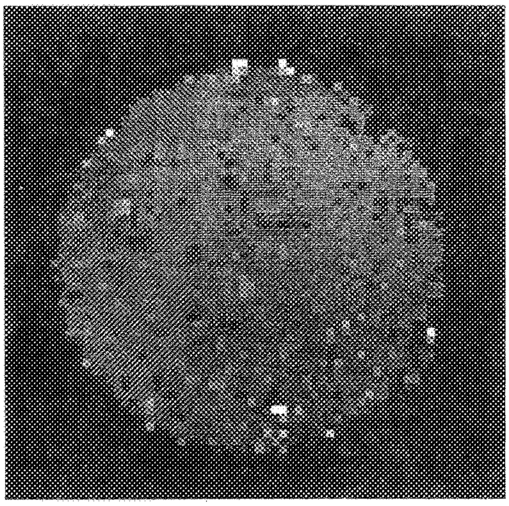

Figure 20 - San Andres Dolomite Slice 4
Positive Flow Image

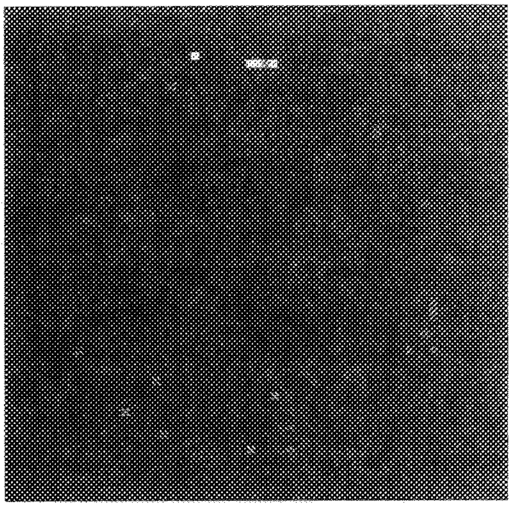

Figure 21 - San Andres Dolomite Slice 4
Negative Flow Image

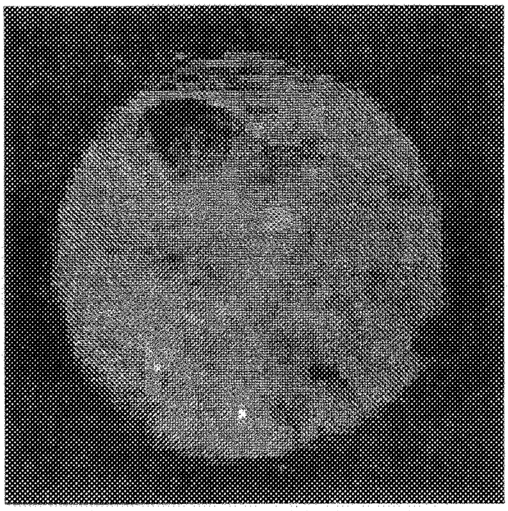

Figure 22 - San Andres Dolomite Slice 7
Magnitude Image

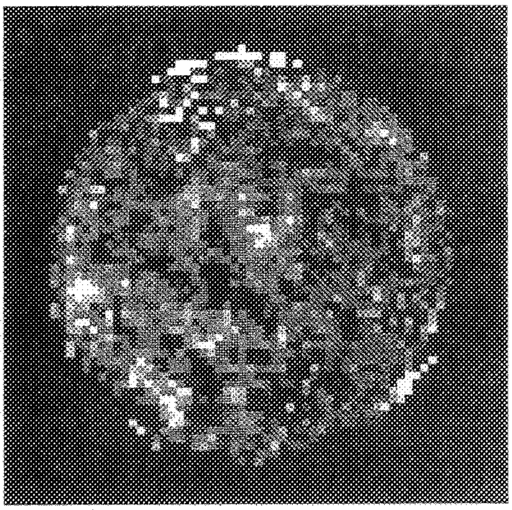

Figure 23 - San Andres Dolomite Slice 7
Positive Flow Image

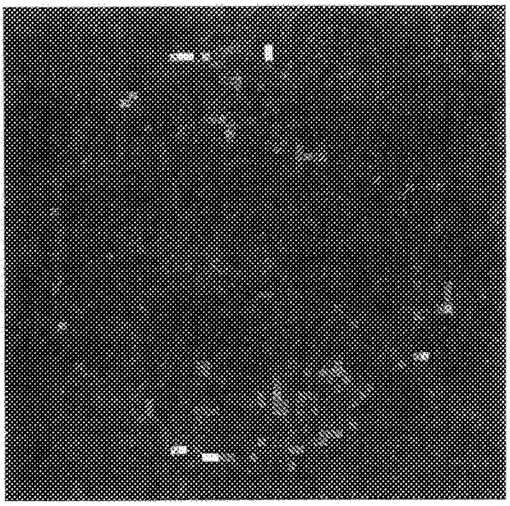

Figure 24 - San Andres Dolomite Slice 7
Negative Flow Image

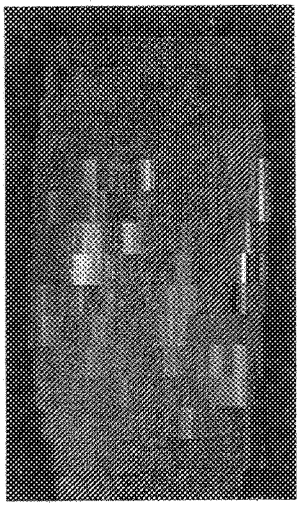

Figure 25 - San Andres Dolomite Sagittal Slice
Magnitude Image

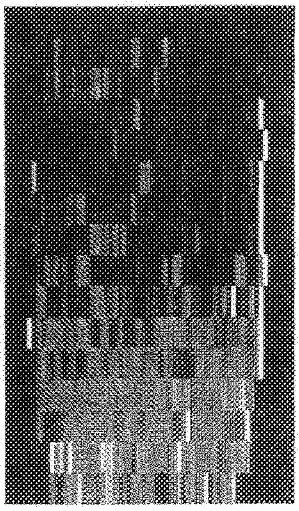

Figure 26 - San Andres Dolomite Sagittal Slice
Positive Flow Image

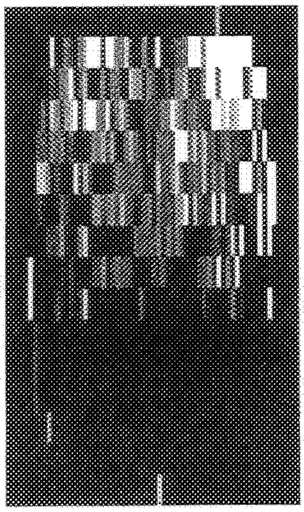

Figure 27 - San Andres Dolomite Sagittal Slice
Negative Flow Image

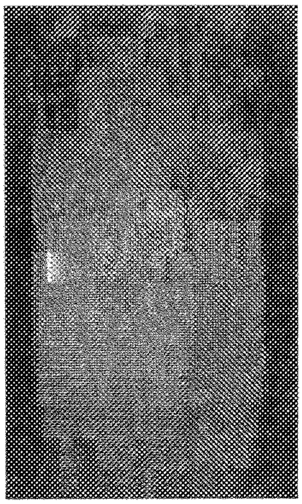

Figure 28 - San Andres Dolomite Coronal Slice
Magnitude Image

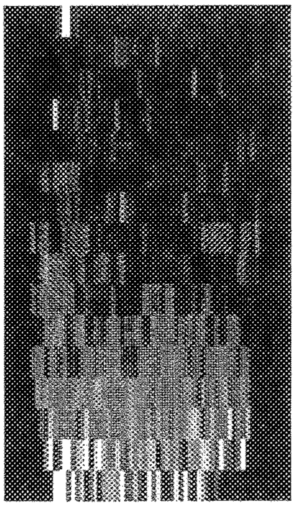

Figure 29 - San Andres Dolomite Coronal Slice
Positive Flow Image

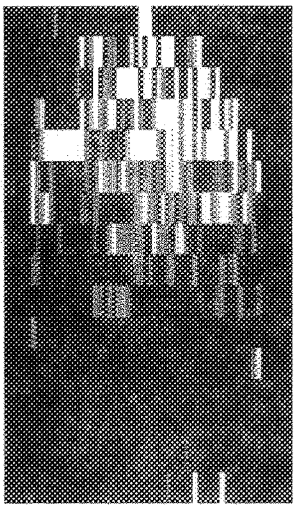

Figure 30 - San Andres Dolomite Coronal Slice
Negative Flow Image